Journal Pre-proofs

Metal Ti quantum chain-inlaid 2D $NaSn_2(PO_4)_3$/H-doped hard carbon hybrid electrodes with ultrahigh energy storage density

Wen He, Changjiu Li, Beibei Zhao, Xudong Zhang, Kwan San Hui, Jiefang Zhu

PII: S1385-8947(20)32439-6
DOI: https://doi.org/10.1016/j.cej.2020.126311
Reference: CEJ 126311

To appear in: *Chemical Engineering Journal*

Received Date: 17 May 2020
Revised Date: 8 July 2020
Accepted Date: 14 July 2020

Please cite this article as: W. He, C. Li, B. Zhao, X. Zhang, K. San Hui, J. Zhu, Metal Ti quantum chain-inlaid 2D $NaSn_2(PO_4)_3$/H-doped hard carbon hybrid electrodes with ultrahigh energy storage density, *Chemical Engineering Journal* (2020), doi: https://doi.org/10.1016/j.cej.2020.126311

Metal Ti quantum chain-inlaid 2D $NaSn_2(PO_4)_3$/H-doped hard carbon hybrid electrodes with ultrahigh energy storage density

Wen He[a,b,*,1], Changjiu Li[b,*,1], Beibei Zhao[a], Xudong Zhang[a,*], Kwan San Hui[c], Jiefang Zhu[d]

[a] *Institute of Materials Science and Engineering, Qilu University of Technology (Shandong Academy of Sciences), Jinan 250353, China.*
[b] *State Key Laboratory of Marine Resource Utilization in South China Sea, Special Glass Key Lab of Hainan Province, Hainan University, Haikou 570228, China.*
[c] *Energy and Environment Laboratory, School of Engineering, University of East Anglia (UEA), Norwich, NR4 7TJ, United Kingdom.*
[d] *Department of Chemistry - Ångström Laboratory, Uppsala University, Box 538, SE-75121 Uppsala, Sweden.*

* Corresponding author.
E-mail address: hewen1960@126.com (W. He), lichangjiu@hainanu.edu.cn (C. Li), zxd@qlu.edu.cn (X. Zhang).
[1] These authors contributed equally to this work and they are all the first complete units.

ABSTRACT

We report the development of a new hybrid electrode that allows for a reinforcing combination of different energy storage mechanisms, providing enhanced energy and power densities. This hybrid electrode is composed of chain-like metal titanium (zero valency state) quantum dots (<10 nm), two-dimension $NaSn_2(PO_4)_3$ layer and H-doped hard carbon layer, and possesses unique sandwich and hierarchically meso-macroporous structures. These chain-like quantum dots are inlaid on the edge of ultra-thin $NaSn_2(PO_4)_3$ nanosheets by using a convenient and economic method, enhancing its conductivity. This design takes advantage of the unique properties of

each component and nanostructure, resulting in synergistic effects to improve the charge transfer and energy storage. The hybrid electrode not only shows high capacity, outstanding rate performance and long cycling stability, but also matches well with porous $Na_3V_2(PO_4)_3$ cathode. Remarkably, the Na/Li mixed-ion full battery exhibits significant improvements on the energy and power densities (555 Wh Kg^{-1}/804 W Kg^{-1} at 1C). Detailed charge storage mechanism investigation reveals that the prelithiation reduces the pseudocapacitive of hybrid electrode and increases its battery behavior, resulting in an ultrahigh energy storage density. Our findings demonstrate that this hybrid electrode is a new potential candidate for high-performance mixed-ion batteries.

Keywords: Metal titanium quantum dot; Sandwich structure; $NaSn_2(PO_4)_3$; Energy density

1. Introduction

Hierarchically porous materials with macropores and mesopores exhibit porosity on two distinct length scales, and therefore combine the benefits of the different pore sizes, which is highly desirable in energy storage [1-3]. The ideal nanostructure materials for future hybrid energy storage devices should be able to transport both electrons and ions efficiently and offer high energy and power densities [4-15]. Rechargeable lithium ion batteries (LIBs) with relatively high energy density as well as long-cycle stability become one of the most promising energy storage systems for electric vehicles and portable electronic devices [16]. However, Li can't be regarded as an abundant

element because of the low mass fraction (~20 ppm) in the earth's crust, resulting into the continuous increase of LIB cost based on the high demand of Li-based raw materials. And lithium metal has safety and low power density issues due to the formation of lithium dendrites [17–19]. To satisfy the rapidly developing market for longer-lasting mobile electronic devices and electric vehicles, developing new alternative energy storage systems with low cost and high energy/power density is extremely urgent [20–23]. Compared to LIBs, sodium-ion batteries (SIBs) offer multiple advantages, such as huge recoverable reserve of Na resource, evenly geographical distribution and distinctly lower cost. SIBs are hence recognized as serious alternative to LIBs [24]. However, research efforts for pure sodium battery systems have encountered numerous problems, such as low reversible capacity, low available power density and insufficient cycle life with rapid capacity decay. The emergence of Li^+/Na^+ mixed-ion batteries (LNMIBs) balances the advantageous features of SIBs and LIBs, which combines the high energy density of LIBs with the safety and low cost of SIBs [25]. Hence, the study of LNMIBs operating at room-temperature has become an important research direction and aroused wide attention.

In design and fabrication of high-performance LNMIBs, the well-matched technology of cathode and anode is highly challenging yet critically important in practical applications. Therefore it is highly imperative to develop superior anode materials with unique structure. Na super ionic conductor (NASICON)-type phosphates have also been widely investigated as anode materials for both Li-ion and

Na-ion batteries because of their open framework structure and unique physical and chemical properties, such as, high ionic conductivity, mechanical stability, thermal stability [26]. Among them, Sn-based phosphates, such as SnP_2O_7 [27,28], $LiSn_2(PO_4)_3$ [29–31], $NaSn_2(PO_4)_3$ [32–34] etc have been considered as a promising alternative to graphite as the anode materials owing to their natural abundance, recyclability, low working potential (less than 0.6 V vs. Li/Li^+), high theoretical capacity (993 mA h g^{-1} for Sn), more than twice of graphite (372 mAh g^{-1}). However, the commercial application of those materials is limited by their low electrical conductivity and rapid capacity fading due to the large volume change during the charge-discharge process.

To improve the electrochemical performances of NASICON-type phosphate anodes, transition metal ion doping has achieved the desired goals. For example, Ti^{4+} [35], Mo^{3+} [36], Cr^{3+} [37], Mg^{2+} [38] and Fe^{3+} [39] can be doped at the V site in the $Na_3V_2(PO_4)_3$. Sn^{4+} [40,41], Fe^{3+} [42] and Al^{3+} [43] can be doped at the Ti site in the $NaTi_2(PO_4)_3$. The results show that these lattice dopings further improved the rate capabilities, electric conductivity, and cyclic stability of anodes. The metal titanium has superconductivity, high plasticity, low chemical activity, high thermal stability and is known as the "third metal" widely used after Fe and Al. However, there is still no report for metal Ti doping in NSP to further improve its electrochemical performances. Besides, 2D materials with sandwich structure, ultrathin thickness and large interlayer spacing can offer some advantages for Na storage, such as inhibiting the stacking of layered materials through the interaction with the carbon component,

shortening the diffusion length of Na ions and facilitating the insertion/extraction of Na ions [44]. In particular, the quantum confinement of electrons in the 2D plane and high exposed contact area impart them with unprecedented electrical and electronic characteristics [45].

Herein, we report a high-performance Na/Li mixed-ion full battery (NLMIFB) based on a new hybrid electrode for the first time. The hybrid electrode is composed of chain-like metal titanium (zero valency state) quantum dots (<10 nm) (Ti-QDs), two-dimension $NaSn_2(PO_4)_3$ (2D-NSP) layer and H-doped hard carbon layer (H-HC). We synthesized the Ti-QDs/2D-NSP/H-HC hybrid electrodes with different Ti additive amount by a simple sol-gel and subsequent calcination method. The challenge of this design is to obtain high-performance LNMIFBs by using the well-matched technology of all phosphate cathode and anode, unique sandwich structure and hierarchically meso-macroporous structure. The hybrid electrode for half cells delivers an ultrahigh initial discharge specific capacity of 1246.5 mAh g^{-1}, superior rate capability (207.5 mAh g^{-1} at 5 A g^{-1}), and high energy density (453 Wh kg^{-1}). These electrochemical performances are among the best thus far reported for NSP (Table S1). Remarkably, the prelithiation full battery assembled by using this hybrid electrode and porous $Na_3V_2(PO_4)_3$ (PNVP) cathode exhibits significant improvements on the energy and power densities (555 Wh kg^{-1}/804 W Kg^{-1} at 1C). Our study provides vital new insights into how to increase the energy and power densities of mixed-ion batteries and develops an effective strategy.

2. Experiment and methods

Preparation of Ti_x-QDs/2D-NSP/H-HC

The raw materials used in this experiment include $SnCl_2•2H_2O$ (98%, Macklin), citric acid (99.5%, Tianjin Damao Chemical Co., Ltd.), $NH_4H_2PO_4$ (99.9%, McLean Reagent Co., Ltd.), Na_2CO_3 (99.9%, McLean Reagent Co., Ltd.), titanium butoxide (99.9%, McLean Reagent Co., Ltd.) and ethanol (99.7%, Tianjin Fuyu Fine Chemical Co.,Ltd). Distilled water was used during the synthesis of the samples.

The Ti_x-QDs/2D-NSP/H-HC samples were prepared by the sol-gel assisted carbon thermal reduction method. The fabrication process of the $T_{0.01}$-QDs/2D-NSP/H-HC sample is illustrated in Fig. S1. Initially, Na_2CO_3 (0.53 g), $NH_4H_2PO_4$ (3.45 g) was dissolved in 20 ml water to form A solution after magnetic stirring for 1 h. $SnCl_2·2H_2O$ (4.49 g) and citric acid (1.05 g) was dissolved in 20 ml water to form B solution after magnetic stirring for 1 hours. Subsequently, titanium butoxide (5 ml) in ethanol (10 ml) were stirred for 1 h to form C solution. Next, C solution (0.11 ml) was added dropwise into B solution under magnetic stirring for 0.5 h. And, A was added the above mixture to form the precursor sol solution. Then, the solvent was evaporated at 80 °C to transform the precursor sol solution to gel. After the transformation, the gel was dried in an oven at 60 °C to form a dry gel precursor and grinded into a fine powder by a grinder. The last step was to anneal the mixture at 350 °C for 5 h and 600 °C for 8 h under N_2 atmosphere to obtain the black sample. Then the black sample washed with distilled water for three times to obtain the

$T_{0.01}$-QDs/2D-NSP/H-HC sample. The other T_xNSP/H-HC samples were synthesized under the same conditions with the different add of the titanium butoxide. The $NaSn_2(PO_4)_3$ (NSP)/C blank sample was also synthesized under the same conditions without adding titanium butoxide. The porous $Na_3V_2(PO_4)_3$ (PNVP) cathode was prepared by using the previously reported method [60].

Material characterization, electrode fabrication and testing are shown in Supplementary S2. The prelithiation process of the $T_{0.01}$-QDs/2D-NSP/H-HC hybrid electrode is illustrated in Fig. S2.

3. Results and discussion

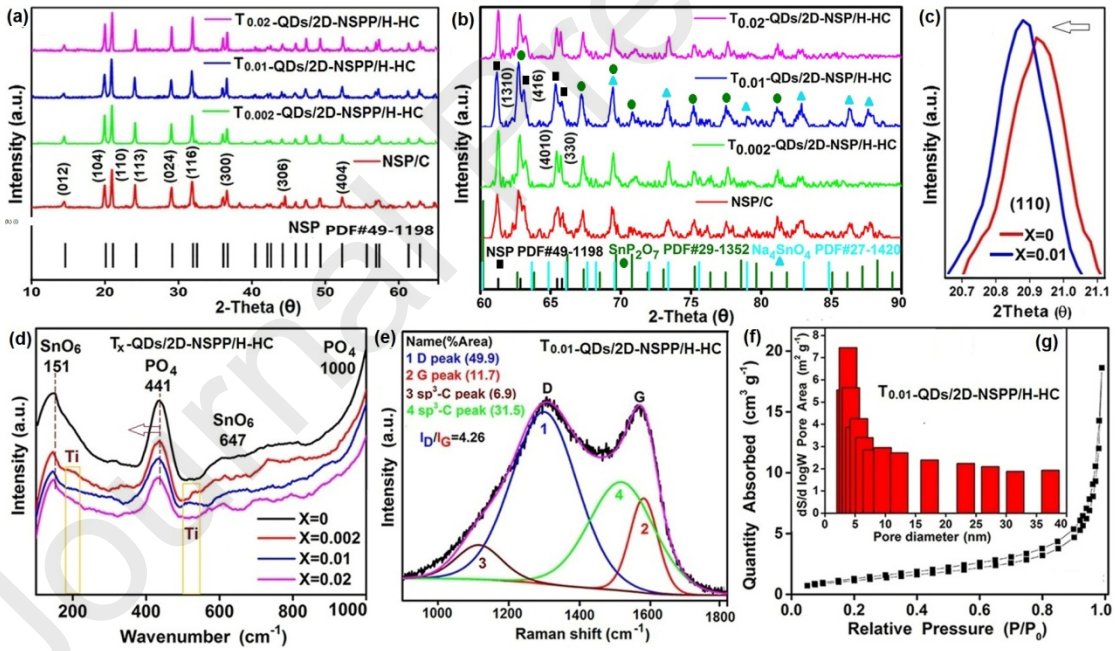

Fig. 1. XRD patterns of different samples over a range of 2θ angle from (a) 10 to 70° and (b) from 60 to 90° (enlarged). (c) diffraction peak contrast of (110) lattice plan. (d) Raman spectra of different samples at a range of low wavenumber from 100 to 1000 cm^{-1} and (e) Raman spectra deconvoluted by four Gaussian peaks of $T_{0.01}$-QDs/2D-NSP/H-HC sample. (f) Nitrogen adsorption-desorption isotherm and (g) BJH pore-size distribution of $T_{0.01}$-QDs/2D-NSP/H-HC sample.

3.1. Characterizations of morphology and structure

First, we characterized the influence of metal Ti doping on the crystal structure of NSP by using X-ray diffraction (XRD) and Raman spectrum. The XRD patterns of the different samples reveal their crystallographic phase and crystallinity (Fig. 1a). It is clear that the sharp and intense peaks of all samples agree well with the standard card (PDF# 49-1198) of $NaSn_2(PO_4)_3$, which indicate that all the samples have well crystallized characteristic of R-3C space group of rhombohedral lattice with a=b=8.507 Å and c=22.467 Å. But there is no distinct characteristic diffraction peaks of Ti because of its low addition amount and amorphous structure, which was confirmed HRTEM image in Fig. S6. In addition, there also is no distinct characteristic diffraction peaks of carbon due to its amorphous structure, which was further confirmed by the results of Raman spectra (Fig. 1e) and HRTEM (Fig. S6). To calculate more precisely lattice parameters, the XRD patterns of different samples in the high angle area of 60–90° are showed in Fig. 1b. Fig. 1b shows that the $T_{0.01}$-QDs/2D-NSP/H-HC sample contains the trace impurity phases of SnP_2O_7 (PDF# 29-1352) and Na_4SnO_4 (PDF# 27-1420). The obvious two peaks located 85-90° appears not in $T_{0.002}$-QDs/2D-NSP/H-HC and $T_{0.02}$-QDs/2D-NSP/H-HC samples because they have less crystallinity. Fig. 1c shows that the (110) diffraction peak shifted toward lower 2θ value due to the metal Ti doping in NSP, proving the increase of its interplanar spacing. Table S2 and S3 present the summary of the lattice parameters calculated by using Jade 6 XRD pattern-processing software, respectively. The results show that the volume of unit cell, the internal tensile strain and the crystal

face distance of (012) for $T_{0.01}$-QDs/2D-NSP/H-HC sample are obviously larger than that of NSP/C blank sample. The evolution of the unit-cell parameters and cell volume are illustrated in Fig. S3a. The change of lattice parameters also indicates that the doping of larger Ti atoms causes the lattice expansion and lattice distortion of NSP (Fig. S16e), which has benefits for facile and fast intercalation/deintercalation of Na/Li mixed-ion and enhancing Na/Li mixed-ion storage [45]. However, the $T_{0.02}$-QDs/2D-NSP/H-HC with higher concentration of titanium atoms doping does not confer better properties than $T_{0.01}$-QDs/2D-NSP/H-HC because of its lower hydrogen content (Table S4), leading to higher R_{ct} and smaller D (Table S7).

In order to furtherly analyze the influence of metal Ti doping on the structure of NSP, Raman spectra of different samples are shown in Fig. 1d. The Raman spectra of all samples show the same main features as the previously published spectrum of $NaSn_2(PO_4)_3$ [34]. The strong peaks around 1000 cm^{-1} can be assigned to the intra molecular stretching modes of PO_4. The strong peaks at 441 cm^{-1} arise from the symmetric bending mode of PO_4. The weak bands at 647 cm^{-1} could be due to the symmetric mode of SnO_6. The strong overlapping peaks at 151 cm^{-1} is lattice modes of SnO_6. The weak bands around 200 and 530 cm^{-1} are transverse acoustic and transverse optical modes of Ti, respectively [46]. Compare with NSP/C sample, two main changes are seen in the Raman spectra of $T_{0.01}$-QDs/2D-NSP/H-HC sample. First, the two strong peaks at both 151 and 441 cm^{-1} shifted toward lower wavenumber (Fig.S3bc), which represent the increase of chemical bond length of P-O and Sn-O, respectively [47]. Second, the vibration intensity of the PO_4 band

significantly weakened. These changes indicate that the metal Ti doping results in the distorting lattice of NSP and further verify the results of XRD, which is also verified by the results of HRTEM (Fig. 3h).

In order to analyze the composition and influences of carbon-wrapped layers, Raman spectra deconvoluted by four Gaussian peaks for $T_{0.01}$-QDs/2D-NSP/H-HC sample are shown in Fig. 1e. It displays two typical peaks located at 1354 and 1595 cm^{-1}, corresponding to the D band (disorder-initiated phonon mode) and G band (graphite mode), respectively. Furthermore, the two broad peaks can be disassembled into four peaks by utilizing Gaussion numerical simulation [48]. The sp3-type carbon (amorphous carbon and the defects) is correlated to two peaks of (1) and (3), while sp2-type carbon (graphitized carbon) is related to the two peaks of (2) and (4) [36]. Meanwhile according to the peak area, the peak intensity ratios of the D-band and the G-band (ID/IG) of $T_{0.01}$-QDs/2D-NSP/H-HC is 4.26, which can be used to determine the amount of defects and disorder in the carbon materials [58]. The carbon contents of different samples are evaluated by using Vario EL IIICHN elemental analyzer (Table S4). The results show that the $T_{0.01}$-QDs/2D-NSP/H-HC sample contains higher hydrogen content and right amount of carbon. The carbon layer mainly originates from the carbonization of citric acid and titanium butoxide in the annealing process (Fig. S16a-c). Fig.1f shows that the nitrogen adsorption-desorption isotherm of $T_{0.01}$-QDs/2D-NSP/H-HC sample, which further studied the porous characteristics. The $T_{0.01}$-QDs/2D-NSP/H-HC sample demonstrates a type-IV isotherm, indicating the existence of mesopores [49]. Its pore size distribution is 2−37 nm (Fig. 1g).

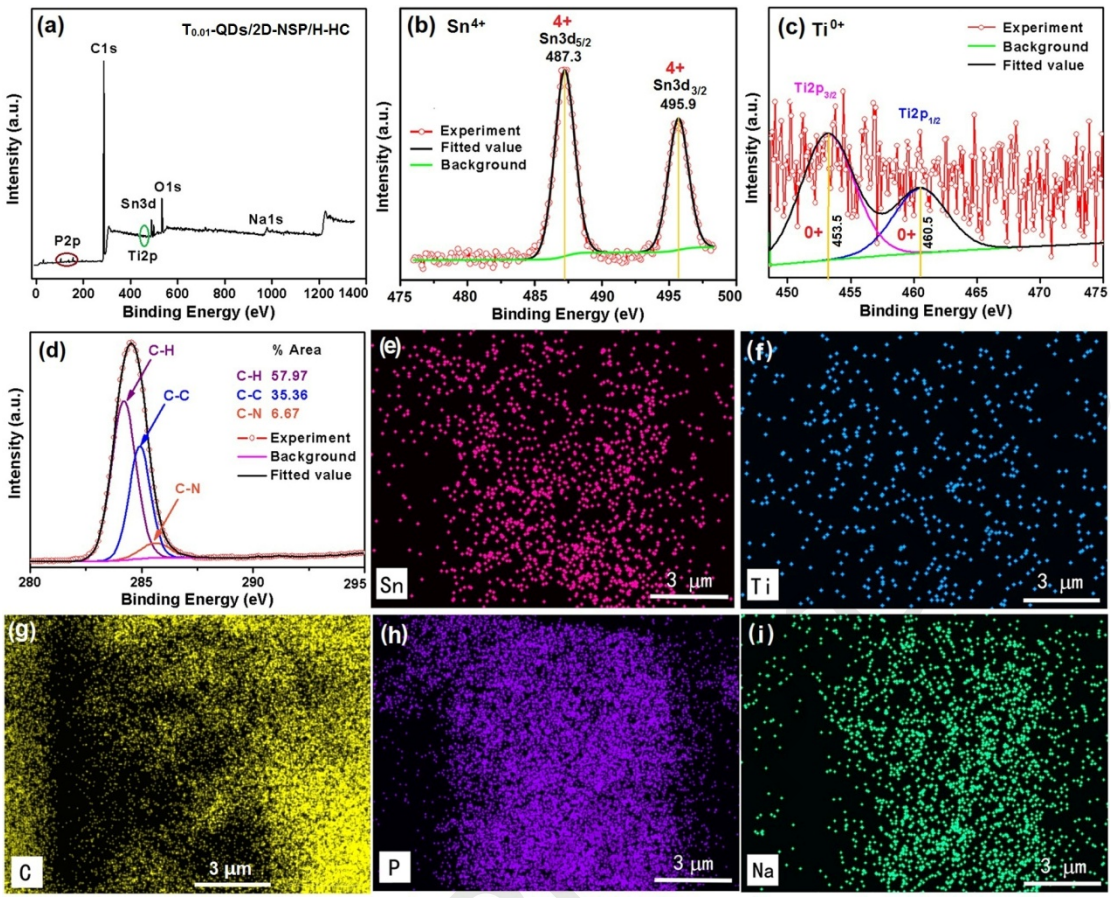

Fig. 2. (a) The full XPS spectrum of $T_{0.01}$-QDs/2D-NSP/H-HC sample. High-resolution XPS spectra of Sn3d (b), Ti2p (c) and C1s (d). (e-i) The elemental mappings of $T_{0.01}$-QDs/2D-NSP/H-HC sample, tin (e), titanium (f), carbon (g), phosphorus (h) and sodium (i).

The X-ray photoelectron spectroscopy (XPS) was carried out to characterize the elemental components and their chemical states. As shown in Fig. 2a, Na, Sn, Ti, P, C and O are discovered in the survey spectrum, which is consistent with the elemental constitute of $T_{0.01}$-QDs/2D-NSP/H-HC sample. The peaks at 487.3 and 495.9 eV in high resolution XPS spectrum of Sn (Fig. 2b) correspond to the $Sn3d_{5/2}$ and $Sn3d_{3/2}$, respectively, which show that the Sn is in a SnO_6 octahedron environment with +4 valency [50]. The high resolution XPS peak at 134.5 eV is related to the P2p (see also Fig. S3d), indicating that the P is in a tetrahedral environment with +5 valance

[51,52]. To validate the valence state of titanium in $T_{0.01}$-QDs/2D-NSP/H-HC, the high resolution XPS spectrum of Ti is presented in Fig. 2c. It is clear that it exhibits double-peak feature with Ti 2p2/3 and 2p1/2 peaks located at 453.5 and 460.5 eV, respectively, which is consistent with the previous studies on TiH_2 and TiN [53,54] and confirms the zero valency of metal Ti doping in $T_{0.01}$-QDs/2D-NSP/H-HC. The high resolution XPS C1s spectrum of $T_{0.01}$-QDs/2D-NSP/H-HC (Fig. 2d) can be resolved into three peaks at 284.20, 284.92, and 285.62 eV, which are assigned to C-H (57.97%), C-C (35.36%), and C-N (6.67%) configurations, respectively [55,56], confirming H-doping in HC layer. However, C-N peak is not obvious, indicating that the content of N-doping in HC layer is relatively fewer. The area of C-H in XPS is larger than that of C-C because more hydroxyl groups from titanium butoxide, citric acid and $NH_4H_2PO_4$ were introduced into the carbon matrix in the synthesis (Fig. S16ab). In addition, elemental mappings of EDS in the SEM image (Fig. S3e) show the uniform distributions of Sn (Fig. 2e), Ti (Fig. 2f), C (Fig. 2g) P (Fig. 2h), Na (Fig. 2j) and O (Fig. S3f) in $T_{0.01}$-QDs/2D-NSP/H-HC. The Ti elements are sparsely distributed in the mapping image (Fig. 2f), which further confirmed the existing of Ti element. Thus, we can conclude that a noticeable amount of H-doping can be formed in situ in hard carbon layer during the synthesis. H-doping is able to induce intrinsic defects that provide free electrons, accordingly improving the electrical conductivity of HC [57,58]. Fig. 4d shows that the rate performance of $T_{0.01}$-QDs/2D-NSP/H-HC is obviously better than that of NSP/C, which further confirms the effects of hydrogen and titanium doping.

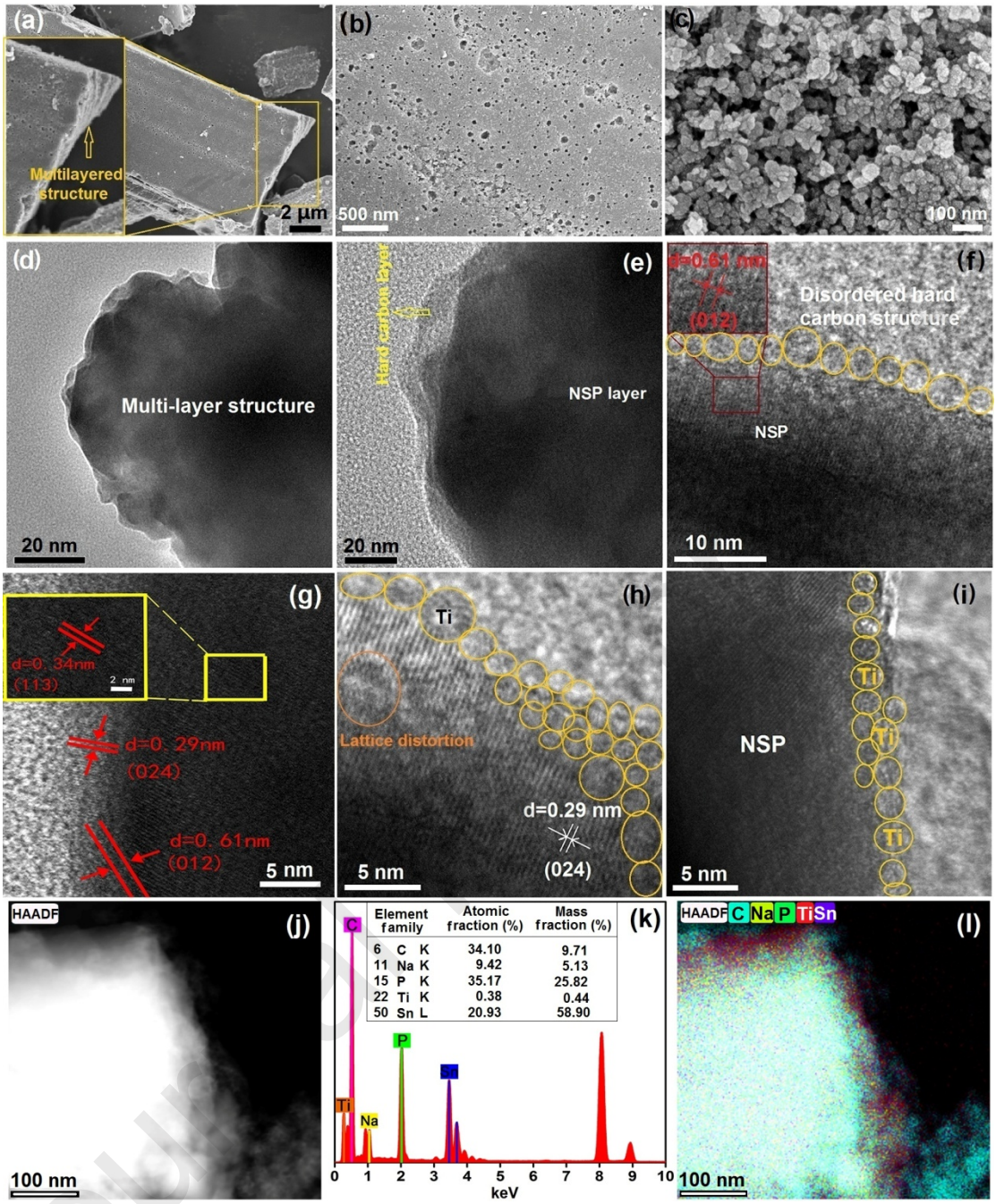

Fig. 3. Morphology and fine texture characterizations of $T_{0.01}$-QDs/2D-NSP/H-HC sample. (a-c) SEM images. (de) TEM images. (f-i) HRTEM images. (j) TEM-EDS image. (k) The corresponding energy spectrum and elemental content. (l) The color mixing elemental mapping image: Ti (red), Na (yellow), Sn (violet), P (green) and C (blue-green).

The morphology and microstructure of the as-prepared samples were investigated by FE-SEM and HRTEM. The SEM images show that the NSP/C blank sample is

consists of many irregular agglomerations of large particles (Fig. S4ab). The $T_{0.002}$-QDs/2D-NSP/H-HC sample is composed of the spherical particles of about 200 nm diameter (Fig. S4cd), while the $T_{0.02}$-QDs/2D-NSP/H-HC sample has tetragonal flake particles (Fig. S4ef). The $T_{0.01}$-QDs/2D-NSP/H-HC sample is composed of many larger layered particles (5 − 50 μm) (Fig. 3a). The inset of Fig. 3a shows clearly the multilayered morphology of a layered particle. Notably, many macropores with a size range of 50−200 nm in this particle are clearly observed in the high-resolution FE-SEM images (Fig. 3bc), which shows that the $T_{0.01}$-QDs/2D-NSP/H-HC sample not only has mesopores (2−50 nm) (Fig.1f), but also macropores. It has been widely recognized that the construction of hierarchical pores of mesopores and macropores is an effective way to improve the electrochemical performances of electrode materials because the macropores provide large diffusion pathways for rapid mass transfer and reservoirs for mass-buffering, and mesopores provide a high surface area [1,59]. The hierarchical pore structure in $T_{0.01}$-QDs/2D-NSP/H-HC sample makes the Na/Li mixed ions and electrolyte easily penetrate and also has a buffering to the volume change of NSP particles. Fig.3c also shows that the large layered particle is formed by the accumulation of many thin slices with a size range from about 20 to 500 nm. These thin slices can shorten the pathway lengths of the mixed ion diffusion effectively during the insertion/extraction processes. The multilayered structure of $T_{0.01}$-QDs/2D-NSP/H-HC is further confirmed by the HRTEM image in Fig. 3d, and worthy of addressing is that the sandwich structure is also observed on the edge of a NSP nanosheet (Fig. 3e and Fig. S5). The disordered hard carbon layer has a light

color contrast due to its smaller atomic weight. Fig.3f shows the clear lattice fringes with lattice spacing (d) of 0.61 nm, corresponding to the (012) crystal plane of NSP nanosheet. The different crystal planes of NSP are shown in Fig.3g. There are distinct lattice dislocations and various defects in Fig. 3h. The metal Ti quantum chains were inlaided on the edge of NSP nanosheet, as shown in Fig. 3f, h and i. These quantum chains are composed of many Ti quantum dots (<10 nm) with different size (see the clearer HRTEM image in Fig. S6). These Ti quantum dots show the relatively shallow image contrast than that of NSP because of smaller atomic weight of Ti. They also show amorphous structure without clear lattice fringes. Fig. 3j and 3k show TEM-EDS image of $T_{0.01}$-QDs/2D-NSP/H-HC sample, the corresponding energy spectrum and elemental content of a thin slice in the nanometer size range, respectively. The color mixing elemental mapping image in Fig. 3l further confirms the distribution location of red Ti element on the edge of the particle. The results of HRTEM indicate that the nucleation and crystal growth of NSP nanosheet occur on the surface of carbon matrix, and Ti ions were reduced by Sn^{2+} during the synthesis to form metal Ti quantum chains on the edge of NSP nanosheet.

3.2. Electrochemical performance evaluation of the half batteries

Optimization studies are carried out for the synthesis of T_x-QDs/2D-NSP/H-HC (x=0, 0.002, 0.01, 0.02) hybrid electrodes by using the galvanostatic charge-discharge test. The electrochemical properties were evaluated in the half batteries assembled with the different anodes synthesized under the different conditions and Li foil

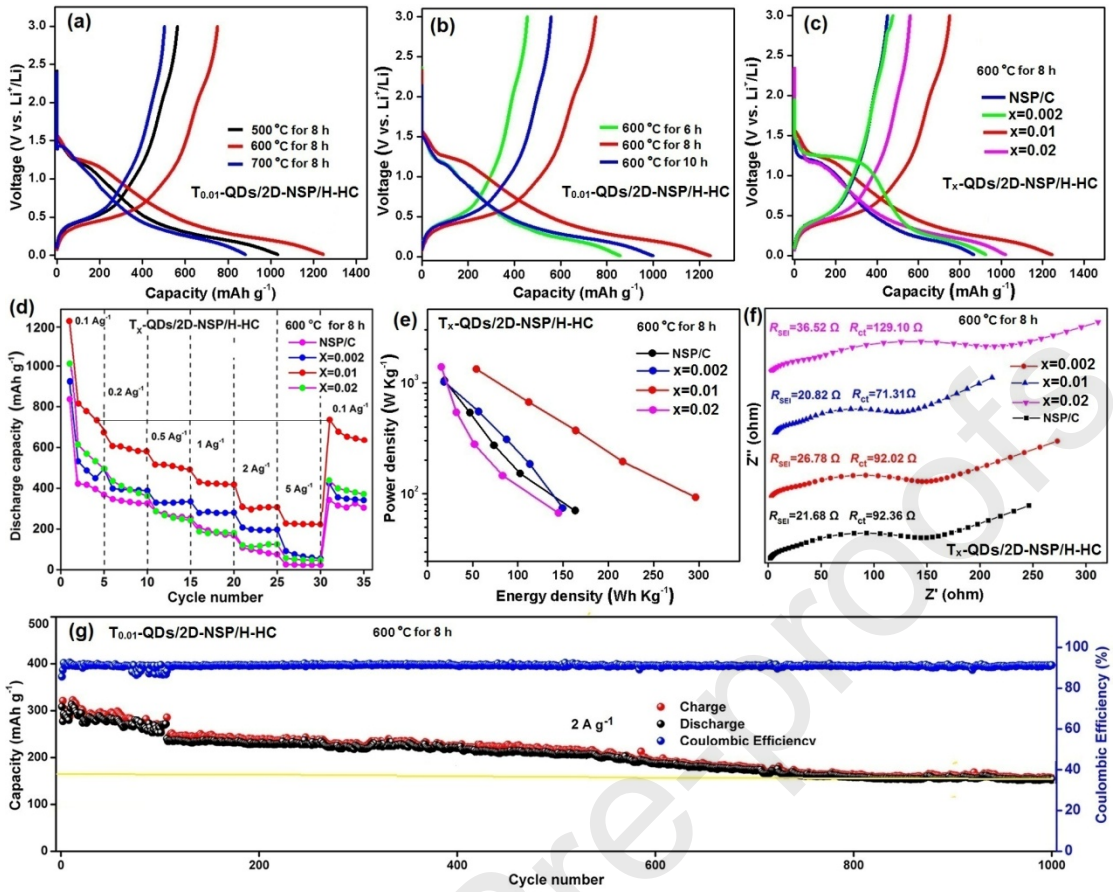

Fig. 4. Electrochemical performance characterizations of the half cells assembled with the T_x-QDs/2D-NSP/H-HC (x=0, 0.002, 0.01, 0.02) hybrid electrodes synthesized under the different conditions and Li foil cathode. The intial charge-discharge curves at 0.1 A g^{-1} for $T_{0.01}$-QDs/2D-NSP/H-HC synthesized with (a) different heat treatment temperature for 8 h, (b) different heat treatment time at 600 °C and (c) different Ti doped content at 600 °C for 8 h. (d) Rate performance of the T_x-QDs/2D-NSP/H-HC from 0.1 A g^{-1} to 5A g^{-1}. (e) Ragone plots (energy density vs. power density) of the T_x-QDs/2D-NSP/H-HC. (f) Nyquist plots of the T_x-QDs/2D-NSP/H-HC. (g) Long cycling performance of the $T_{0.01}$-QDs/2D-NSP/H-HC at 2 A g^{-1}.

cathode. Fig. 4a-d and Figs. S7-S8 exhibit the initial discharge-charge curves and the rate performances of different hybrid electrodes, respectively. The results show that the $T_{0.01}$-QDs/2D-NSP/H-HC hybrid electrode synthesized at 600 °C for 8 h has the best electrochemical performances because of appropriate Ti atom, crystallization degree and crystalline size (Table S2) as well as the unique nanostructure (Fig. 3).

The $T_{0.01}$-QDs/2D-NSP/H-HC synthesized under the optimized conditions exhibits a ultrahigh initial discharge specific capacity of 1246.5 mAh g^{-1} and superior rate capability than that of other anodes. When the current density is 0.5, 2 and 5 A g^{-1}, the discharge capacity of $T_{0.01}$-QDs/2D-NSP/H-HC is 531.1, 336.9 and 207.5 mAh g^{-1} respectively (Fig. 4d). Furthermore, the cycling curve of $T_{0.01}$-QDs/2D-NSP/H-HC at the small current density of 0.1 A g^{-1} after several cycles exhibits that it was only recovered to the discharge capacity (739.41 mA h g^{-1}) of the fourth cycle, which is due to the formation of inactive tin clusters during subsequent cycling under different large current density [30].

The CV curves of $T_{0.01}$-QDs/2D-NSP/H-HC at the different rate for the first three cycles are shown in Fig. S9ab. Fig. S9a, a pair of obvious redox peaks locates respectively at about 0.05 and 0.51 V, which correlates to the reversible redox reactions of NSP. An reduction peak at 1.03 V is observed at the first cycle and then disappears in the following cycles due to the formation of solid electrolyte interface (SEI) film on the anode surface [28]. The formation of SEI film causes an irreversible capacity loss of 39.6% in the first cycle (Fig.S9c). Moreover, the faster scanning rate causes some small peaks to shift (Fig.S9b) and disappear (Fig. 6a). The CV curves at the rate of 0.5 mV s^{-1} after two cycles become stable (Fig.S9b). The charge-discharge profiles at the rate of 0.1 A g^{-1} for the first three cycles (Fig.S9c) are in good agreement with the CV results in Fig.S9a. The rate performance of citric acid carbon anode after pyrolysis at 600 °C for 8 h (Fig. S10) is very poor and barely has capacity at the high rate of 5 A g^{-1}.

The energy and power densities of the different electrodes are calculated from the discharge curves at various current densities (Equation S2). Fig. 4e shows the Ragone plot (energy density vs. power density) of different electrodes in the voltage range of 0–3.0 V. The results show that $T_{0.01}$-QDs/2D-NSP/H-HC has better energy density and power density than other electrodes, showing a high energy density of 453 Wh kg^{-1} at a power density of 58.6 W kg^{-1} (0.1 A g^{-1}), which also remains 54.5 W h kg^{-1} even at an ultrahigh power density of 1315 W kg^{-1} (5 A g^{-1}) (further details are presented in Table S5). Furthermore, the long-life performances of different electrodes at a current density of 2 A g^{-1} are shown in Fig. 4g and Fig. S11, respectively. The results indicates that the $T_{0.01}$-QDs/2D-NSP/H-HC has more excellent cycling performance than that of other electrodes. It not only displays a high discharge capacitie of 315 mA h g^{-1} at first cycle, but also has high Coulombic efficiency of 95% and the discharge capacity retention rate of 55% after 1000 cycles (Table S6). The discharge capacity of $T_{0.01}$-QDs/2D-NSP/H-HC is 173.25 mA h g^{-1} over 1000 cycles (Fig. 4g), which is among the best thus far reported for NSP (Table S1). Additionally, the cycling curve significantly breaks off after 100 cycles in the Fig. 4g, which is attributed to the self-discharge phenomenon of the battery caused by a power failure in the test facility. The specific capacity of other three contrast samples rises at initial several cycles in Fig. S11, such behavior can be attributed to the initial activation of electrodes. However, this phenomenon is not observed in the $T_{0.01}$-QDs/2D-NSP/H-HC sample (Fig. 4g) because it has been activated at the lower current density.

The Nyquist plots of different electrodes are composed of two depressed semicircles at high and medium frequency regions and an inclined straight line at low frequency regions (Fig. 4f). According to the surface layer model [60], a dot (ohmic resistance R_e) on the ultrahigh frequency region of the horizontal axis is electron resistance of the active material. The first semicircle in the high frequency region can be assigned to the resistance (R_{SE}) of Na/Li mixed-ion diffusion via solid electrolyte interphase (SEI), while the second semicircle in the medium frequency region represents charge transfer resistance (R_{ct}) between the electrolyte and electrode. The sloping lines in the low frequency region are attributed to the Warburg impedance of mixed-ion diffusion in the solid phase. Fig. S12 shows the relationship between Z' and $\omega^{-1/2}$ of the different electrodes. A linear characteristic could be seen for every curve. Furthermore, the diffusion coefficient (D) of Na/Li mixed-ions can be calculated from the plots in the low frequency region based on the S3 and S4 equations, and the correspondence parameters calculated using the Zview software are summarized in Table S7 [61]. The $T_{0.01}$-QDs/2D-NSP/H-HC not only has the smallest R_{SEI} (20.82 Ω) and R_{ct} (71.31 Ω), but also the largest ion diffusion coefficient (D=1.38×10^{-14} cm^2 s^{-1}), which is much higher than that (D=2.64×10^{-15} cm^2 s^{-1}) of NSP/C. The results imply that the conductivity, rate of ion diffusion and charge transfer are effectively improved by moderate metal Ti doping and H doping. Fig. S13 show the photos of powered LEDs using the different T_x-QDs/2D-NSP/H-HC (x=0, 0.002, 0.01, 0.02) half cells.

3.3. Electrochemical performance evaluation of Na/Li mixed-ion full batteries

To fully reveal the potential application and expatiate the energy storage mechanism, the Na/Li mixed-ion full batteries were assembled by using the $T_{0.01}$-QDs/2D-NSP/H-HC as anode and the porous $Na_3V_2(PO_4)_3$ (PNVP) as cathode. The prelithiation of the anode is carried out for tuning the electrochemical performances and achieving remarkable energy and power density values (see the prelithiation process in Fig. S2) [62]. Table S8 lists the magnification of the $T_{0.01}$-QDs/2D-NSP/H-HC//PNVP full battery and the corresponding current densities of the cathode and the anode in the voltage range of 1.0−4.0 V. The electrochemical performances of the full batteries before and after prelithiation are shown in Fig. 5. By contrast, it can be seen that the luminosity of the lit LED bulb driven by the full battery after prelithiation (Fig. 5c) is significantly higher than that of LED bulb before prelithiation (Fig. 5a). Fig. 5d shows that the full battery after prelithiation has better rate capability and higher charge-discharge voltage plateaus (3.65/3 V) than that of the full battery before prelithiation (Fig. 5b). The initial discharge and charge capacities of $T_{0.01}$-QDs/2D-NSP/H-HC//PNVP full battery after prelithiation are 444.8 and 478.2 mAh g^{-1} at the rate of 0.1 C, respectively. The higher charge-discharge voltage plateaus would promote its energy/power densities. Meanwhile, the overpotential between discharging/charging profiles is about 0.65 V, reflecting the good reaction kinetics [28]. Fig. 5e reveals that the full battery after prelithiation has excellent rate performance at the rates from 0.1 to 2 C, and the discharge capacity of 176.8 mAh g^{-1} can be maintained at 2 C. Compared with the full battery before prelithiation, the energy and power densities of the full battery after prelithiation have

also been tremendously improved (Fig. 5f) due to the enhanced contribution of battery behavior (Fig. 6i) and improved phase change and redox reactions of NSP

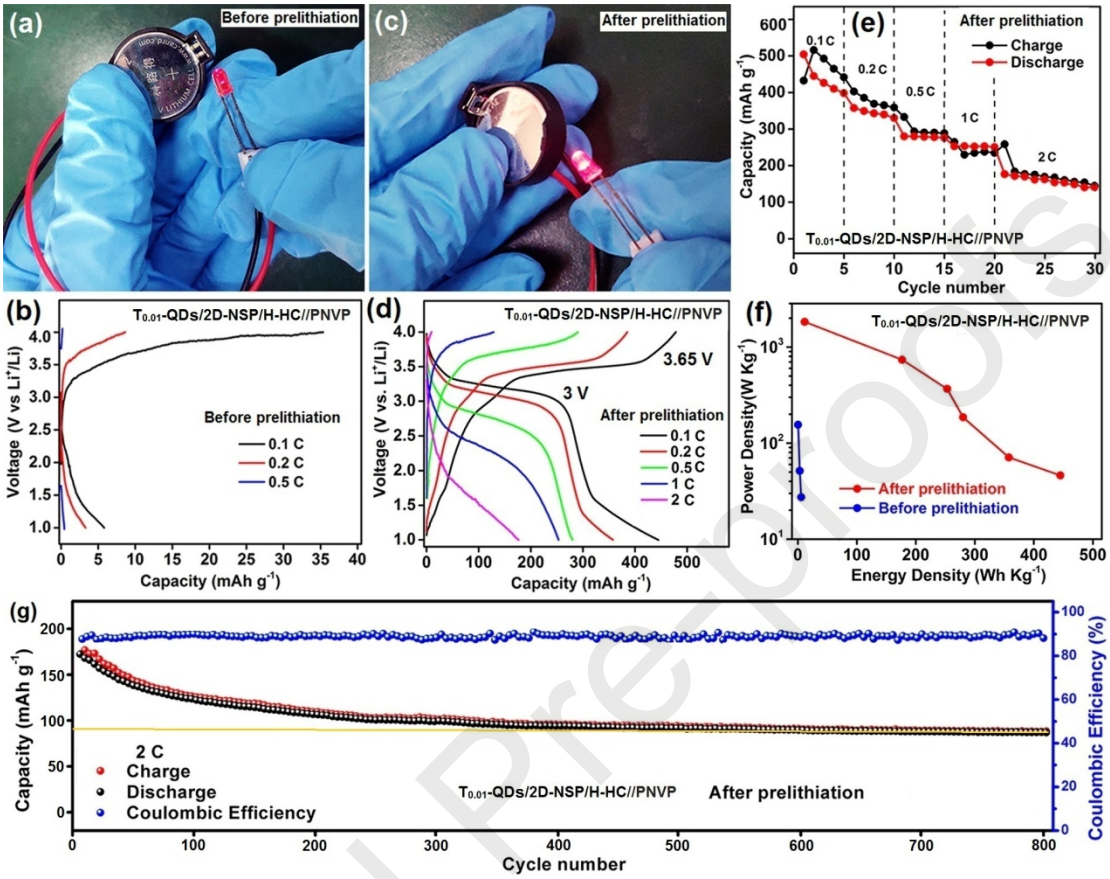

Fig. 5. Electrochemical performance comparison of $T_{0.01}$-QDs/2D-NSP/H-HC//PNVP full batteries before and after prelithiation. (ac) Photos of brightness contrast of the lit LED bulb driven by the full batteries. (bd) Charge and discharge curve contrast. (e) Rate performance of the full battery after prelithiation. (f) Ragone plot comparison of energy and power density. (g) Long cycling performance of the full battery after prelithiation at 2 C.

(Fig. S16h). The full battery before prelithiation has lower energy and power densities (Table S9), but the full battery after prelithiation can achieve both ultrahigh energy and power densities (1147 Wh kg^{-1}/119 W kg^{-1} and 294 Wh kg^{-1}/1226 W kg^{-1}) (Table S10). Fig. 5g is long cycling performance of the full battery after prelithiation for 800 cycles at a current density of 2 C. The full battery runs well after the first charge process and retains the Coulombic efficiency nearly 90% after

800 cycles, demonstrating its splendid reversibility. Table S11 presents the comparison of electrochemical properties of various Na/Li mixed-ion battery in this work.

To further investigate the well-matched effect between cathode and anode, both the electrochemical tests of Na-ion half cell fabricated using PNVP as cathode and the CV measurements of different cells were carried out. Fig. S14ab shows that the Na-ion half cell exhibits superior rate capability (Fig. S14a) and excellent cycling performance (Fig. S14b). The CV curve of the Na-ion half cell and the Li-ion half cell used $T_{0.01}$-QDs/2D-NSP/H-HC as anode and Li foil as cathode were displayed in Fig. S14cd, respectively. The results show that they all delivered the weak polarization of the electrochemical reaction in the battery. In the potential range of 2.4–4.2 V, the Na half cell has higher working potential (high than 3.0 V vs. Na/Na^+) (Fig. S14c), while the $T_{0.01}$-QDs/2D-NSP/H-HC//Li half cell has lower working potential (less than 0.6 V vs. Li/Li^+) in the potential range of 2.5–0.0 V (Fig. S14d). The CV curve of $T_{0.01}$-QDs/2D-NSP/H-HC shows a discharge voltage plateau appears at 0.05 V and a charge voltage plateau appears at 0.51 V, which correspond to the alloying and dealloying process [28]. With an increasing scan rate, anodic potential shifts to higher voltages and the cathodic potential shifts to lower voltages, indicating an increased polarization at the higher sweep rates (Fig. S9b). Fig. S14e is the CV curve of $T_{0.01}$-QDs/2D-NSP/H-HC//PNVP full battery after prelithiation at 0.1 mV s^{-1} in the voltage range of 2.0−4.5, showing a pair of well-defined redox peaks at 3.65/3.0 V correspond to the phase changes during the intercalation and de-intercalation of Na/Li

mixed ions, which is consistent with the charge-discharge voltage plateaus (Fig. 5d). This full battery reaction exhibits excellent reversibility due to the well-matched effect beween cathode and anode.

3.4. Mechanism evaluation

To understand the energy storage mechanisms of different batteries, the CV curves are be used to identify the battery behavior and pseudocapacitive behavior. The capacitive contributions of total stored charge and the adjustable parameter b can be calculated using the S5 and S6 equations, respectively. b=0.5 reflects a diffusion-controlled process of batteries, while b=1.0 implies a surface-controlled process of supercapacitors. Generally, b value locates between 0.5 and 1.0, suggesting a mixed contribution of both processes [63]. As shown in Fig. 6a and Fig. 6d, the CV curves of the half cell and the full battery before prelithiation basically keep the shape and contour at different sweep rates, indicating the same electrochemical reactions. When the scanning rate is 1.0 mV s^{-1}, the CV curve of the full battery after prelithiation shows a clear pair of redox peaks (Fig. 6g), which indicates that its charge storage mechanism is controlled by the diffusion-controlled process of the PNVP cathode (Fig. S14c). However, with the scanning rate increases, this pair of redox peaks gradually disappeared because the pseudocapacitive behavior of $T_{0.01}$-QDs/2D-NSP/H-HC anode. When the scanning rate exceeds 1.0 mV s^{-1}, the CV curves of the full batteries before and after prelithiation all show the nearly rectangular morphology without distinct redox peaks (Fig. 6d and Fig. 6g), which

verify that they all have the pseudocapacitive behavior at higher scanning rates. This is similar to the characteristic of a surface-confined charge transfer process of electric

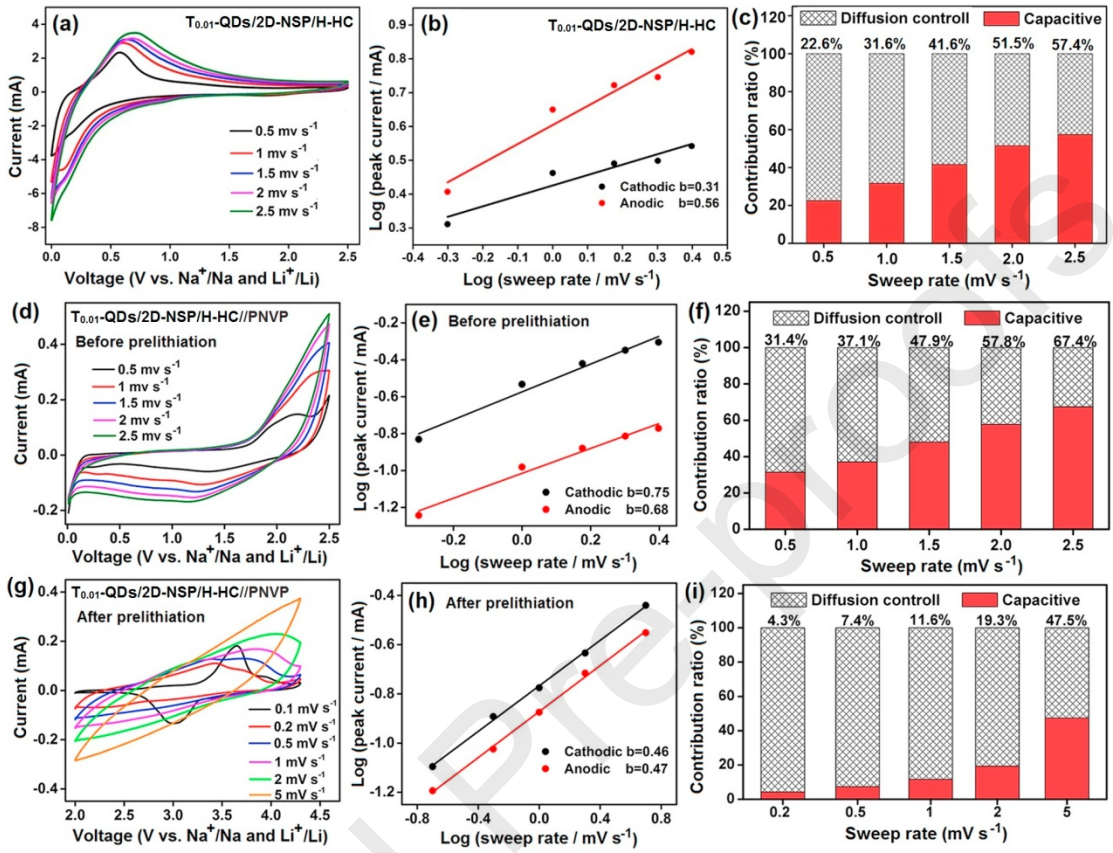

Fig. 6. The energy storage mechanism of different batteries. (a) The CV curves, (b) plots of log (sweep rate) versus log (peak current) and (c) capacitive contribution of the half cell assembled with the $T_{0.01}$-QDs/2D-NSP/H-HC anode and Li foil cathode at various sweep rates. (d) The CV curves, (e) plots of log (sweep rate) versus log (peak current) and (f) capacitive contribution of the $T_{0.01}$-QDs/2D-NSP/H-HC//PNVP full battery before prelithiation at various sweep rates. (g) The CV curves, (h) plots of log (sweep rate) versus log (peak current) and (i) capacitive contribution of the $T_{0.01}$-QDs/2D-NSP/H-HC//PNVP full battery after prelithiation at various sweep rates.

---

double layer (EDL) capacitors [64,65]. The area of rectangular CV curves increases as increasing the scanning rate. The b-values of the cathode and anode peaks for the half cell, the full batteries before and after prelithiation are shown in Fig. 6b, Fig. 6e and Fig. 6h, respectively. Using the equation S7, we can identify the capacity contribution from capacitive and diffusion-controlled charge in the entire potential window. With

the increase of scanning rate, the contribution of capacitive charge for all batteries increases. The results show that the half cell mainly displays the battery behaviour due to the lower *b*-values (Fig. 6b) and the lower capacity contribution (Fig. 6c), reflecting that its charge storage mechanism is controlled by the diffusion-controlled process of Na/Li mixed-ions in the bulk of $T_{0.01}$NSP by means of redox reactions, and hence the high discharge capacity (828.98 mAh g^{-1}) and ultrahigh energy density (453.37 Wh Kg^{-1}) (Table S5) can be achieved at a current density of 0.1 A g^{-1}. The full battery before prelithiation has the higher *b*-values (Fig. 6e) and the higher capacity contribution (Fig. 6f) at high scanning rate, showing the pseudocapacitive behaviour of surface-controlled process by adsorption and electrostatic accumulation of charges in sandwich framework structure and hierarchical pore structure (Fig. 6g). However, both *b* values and contributions of the full battery after prelithiation are significantly reduced than that of the full battery before prelithiation. The $b<0.5$ values (Fig. 6h) and the biggest contribution of 47.7% (Fig. 6i) all reflect that the prelithiation significantly increased the contribution of battery behavior and improved phase change and redox reactions of NSP (Fig.S16h). So the ultrahigh energy and power densities of full battery after prelithiation can be achieved (Table S10).

Based on the results of structure characterizations and electrochemical performance analysis, the synthetic mechanism of $T_{0.01}$-QDs/2D-NSP/H-HC, the ion exchange mechanism of Na/Li mixed ions and the energy storage mechanisms before and after prelithiation are proposed as shown in the Fig. S16. In the synthesis of $T_{0.01}$-QDs/2D-NSP/H-HC, Sn ion solution, titanium butoxide solution, Na_2CO_3 and

$NH_4H_2PO_4$ were mixed to form the precursor made of sol-gel matrix and H-doped carbon matrix (Fig. S16ab). Fig. S15 shows the XRD pattern of $T_{0.01}$-QDs/2D-NSP/H-HC precursor sample before calcination, which matched well with that of $Sn^{2+}HPO_4$ (PDF no. 70-1288), Sn^{4+} $(HPO_4)_2(H_2O)$ (PDF no. 83-0110) and $NaTi^{3+}P_2O_7$ (PDF no. 84-1736). The results show that the redox reaction that occurs during synthesis as following:

$$Sn^{2+} + 2Ti^{4+} = Sn^{4+} + 2Ti^{3+} \quad (1)$$

In the carbothermal reduction reaction protected by nitrogen, this redox reaction continues:

$$3Sn^{2+} + 2C + N_2 + O_2 + 2Ti^{3+} = 3Sn^{4+} + 2CO + N_2 + 2Ti^{0+} \quad (2)$$

After the heat treatment the added titanium is completely reduced to the chain-like metal titanium (zero valency state) quantum dots and the H-doped carbon matrix is converted to H-doped hard carbon layer. The layer-structured $T_{0.01}$-QDs/2D-NSP/H-HC was obtained simultaneously (Fig. S16c). Importantly, this novel sandwich structure provides multiple advantages: (1) the ultrathin layer structure of NSP nanosheets provides shorten the solid-state ion/electron transport path to enhance rate capability, as shown Fig. S16d. (2) The metal Ti quantum dots have many good properties, such as chemical stability, superconductivity and high plasticity, so the metal Ti doping in NSP can increase much more active sites by lattice expansion to increase capability. Fig. S16e shows the influence of metal Ti doping on the crystal structure of NSP as shown by our calculations (see Table S2). (3) The unique sandwich structure could be used as a stable scaffold for more ion

storage sites, fast electron transmission and ion migration, which is the most significant factor for ultrahigh rate performance and excellent long cycling life. (4) H-doping in hard carbon can adjust the surface functional groups of hard carbon, enhancing electric conductivity, in favor of the charge transfer and hybrid electrode–electrolyte interactions [58].

The ion exchange and insertion/extraction reactions of Na/Li mixed ions in the processes of charging and discharging can be presented as below equations:

$$NaSn_2(PO_4)_3 + xLi^+ \rightarrow Na_{1-x}Li_xSn_2(PO_4)_3 + xNa^+ \quad (3)$$

$$Na_3V_2(PO_4)_3 + xLi^+ \rightarrow Na_{1-x}Li_xV_2(PO_4)_3 + xLi^+ \quad (4)$$

$$Na_{1-x}Li_xSn_2(PO_4)_3 + (8-x)Li^+ + xNa^+ 8e^- \rightarrow 3Li_{3-x}Na_xPO_4 + 2Sn \quad (5)$$

$$5Sn + (22-x)Li^+ + xNa^+ + 22e^- \leftrightarrow Li_{22-x}Na_xSn_5 \quad (6)$$

here, Na/Li mixed-ion electrolyte is formed by ion exchange during the charge/discharge process. During the discharging process, Na^+ ions were extracted from $T_{0.01}$-QDs/2D-NSP/H-HC hybrid electrode into the electrolyte by ion exchange with Li ions in the electrolyte and some Li^+ ions were also inserted in the PNVP cathode as shown in Fig. S16f. During the charging process, Na^+ ions were extracted from PNVP cathode into the electrolyte by ion exchange, the Li^+/Na^+ mixed-ions are transferred through the electrolyte and inserted in the $T_{0.01}$-QDs/2D-NSP/H-HC anode and PNVP cathode, respectively. $Li_{3-x}Na_xPO_4$ with high ionic conductivity is formed during the charge/discharge process. Moreover, the Ti doping, hydrogen doping and sandwich structure can greatly enhance the transports of Li^+/Na^+ mixed-ions and electrons to keep the charge balance and relieve the strain caused by the volumetric

change.

4. Conclusion

In summary, through metal Ti doping, hydrogen doping, appropriate nanostructure design and prelithiation of hybrid electrode, we have successfully developed a new Li/Na mixed-ion full battery (LNMIFB) with ulteahigh energy and power densities. A series of T_x-QDs2D-NSP/H-HC (x=0，0.002，0.01 and 0.02 mol%) hybrid electrodes are prepared and the synthesis conditions are optimized. The results show that the metal Ti-doping, hydrogen doping, sandwich structure and hierarchical pore structure would be beneficial for the shuttling of electrons and Na/Li mixed-ions, the stability of architecture, enhancing the rate capability and cycle stability. The $T_{0.01}$-QDs/2D-NSP/H-HC hybrid electrode for half cells exhibits a ultrahigh initial discharge capacity (1246.5 mAh g^{-1} at 0.1 Ag^{-1}), excellent high-rate capacity (207.5 mAh g^{-1} at 5.0 A g^{-1}), long cycling stability and Coulombic efficiency retention (173 mA h g^{-1} and 95% over 1000 cycles at 2.0 A g^{-1}). Moreover, because the $T_{0.01}$-QDs/2D-NSP/H-HC can well-match with the PNVP cathode, the full-battery after prelithiation exhibits significant improvements on the energy and power densities (555 Wh Kg^{-1}/804 W Kg^{-1} at 1C) as well as long cycling stability (93 mA h g^{-1} over 800 cycles at 2C). This elaborate work might open up a potential avenue for the rational design of hybrid electrodes for high-performance Na/Li mixed-ion full batteries.

Appendix A. Supporting information

Supplementary data associated with this article can be found in the online version at http://

Acknowledgements

The authors thank National Natural Science Foundation of China (Grant No. 51672139, 51472127 and 51702177) for the financial support.

Author contributions

W.H. C. L. and X.Z. conceived the research and designed the work. B.Z. performed the synthesis, characterization and electrochemical measurements of the materials. K.H. and J.Z. coordinated the experimental work and performed HRTEM and XPS spectrum experiments. W.H., C. L. and X.Z. edited and finalized the manuscript. All authors discussed the results and commented on the manuscript.

Competing financial interests

The authors declare no competing financial interests.

References

[1] S. Kim, J. Lee, Spinodal Decomposition: A New Approach to Hierarchically Porous Inorganic Materials for Energy Storages, Natl. Sci. Rev. nwz217 (2019) https://doi.org/10.1093/nsr/nwz217.

[2] W. G. Lim, S. Kim, C. Jo, J. Lee, A Comprehensive Review of Materials with Catalytic Effects in Li-S Batteries: Enhanced Redox Kinetics, Angew. Chem. Int. Ed. 58 (2019) 2–14.

[3] S. Kim, M. Ju, J. Lee, J. Hwang, J. Lee, Polymer Interfacial Self-Assembly Guided Two-dimensional Engineering of Hierarchically Porous Carbon Nanosheets, J. Am. Chem. Soc. 142 (2020) 9250–2957.

[4] R. Röder, S. Geburt, M. Zapf, D. Franke, M. Lorke, T. Frauenheim, A. Luisa da Rosa, C. Ronning, Transition Metal and Rare Earth Element Doped Zinc Oxide Nanowires for Optoelectronics, Advanced Science 256 (2019) 1800604.

[5] M. R. Lukatskaya, B. Dunn, Y. Gogotsi, Multidimensional materials and device architectures for future hybrid energy storage, Nat. Commun. **7** (2016) 12647.

[6] D. Zhao, H. Liu, X. Wu, Bi-interface induced multi-active MCo_2O_4@MCo_2S_4@PPy (M=Ni, Zn) sandwich structure for energy storage and electrocatalysis, Nano Energy 57 (2019) 363-370.

[7] X. Wu, S. Yao, Flexible electrode materials based on WO_3 nanotube bundles for high performance energy storage devices, Nano Energy 42 (2017) 143-150.

[8] D. Zhao, X. Wu, C. Guo, Hybrid MnO_2@$NiCo_2O_4$ nanosheets for high performance asymmetric supercapacitors, Inorg. Chem. Front. 5 (2018) 1378-1385.

[9] D. Zhao, M. Dai, H. Liu, L. Xiao, X. Wu, H. Xia, Constructing High Performance Hybrid Battery and Electrocatalyst by Heterostructured $NiCo_2O_4$@NiWS Nanosheets, Cryst. Growth Des. 19 (2019)1921-1929.

[10] D. Zhao, M. Dai, H. Liu, K. Chen, X. Zhu, D. Xue, X. Wu, J. Liu, Sulfur-Induced Interface Engineering of Hybrid $NiCo_2O_4$@$NiMo_2S_4$ Structure for Overall Water Splitting and Flexible Hybrid Energy Storage, Adv. Mater. Interfaces 6 (21) (2019)1901308.

[11] H. Liu, D. Zhao, Y. Liu, P. Hu, X. Wu, H. Xi, Boosting energy storage and electrocatalytic performances by synergizing $CoMoO_4$@$MoZn_{22}$ core-shell structures, Chem. Eng. J. 373 (2019) 485-492.

[12] C. Liu, X. Wu, B. Wang, Performance modulation of energy storage devices: A case of Ni-Co-S electrode materials, Chem. Eng. J. 392 (2020) 123651.

[13] C. Xiong, B.Li, H. Liu, W. Zhao, C.Duan, H. Wu, Y. Ni, A smart porous wood-supported flower-like NiS/Ni conjunction with vitrimer co-effect as a multifunctional material with reshaping, shape-memory, and self-healing properties for applications in high-performance supercapacitors, catalysts, and sensors, J. Mater. Chem. A (2020) doi:10.1039/D0TA03664A.

[14] C. Xiong, M. Li, W. Zhao, C. Duan, L. Dai, M. Shen, Y. Xu, Y. Ni, A smart paper@polyaniline nanofibers incorporated vitrimer bifunctional device with reshaping, shape-memory and self-healing properties applied in high-performance supercapacitors and sensors, Chem. Eng. J. 396 (2020) 125318.

[15] C. Xiong, M. Li, W. Zhao, C. Duan, Y. Ni, Flexible N-Doped reduced graphene oxide/carbon Nanotube-MnO_2 film as a Multifunctional Material for High-Performance supercapacitors, catalysts and sensors, J. Materiomics 6 (3)

(2020) 523–531.

[16] Y. Zhang, P. Wang, G. Li, J. Fan, C. Gao, Z. Wang, Y. Yue, Clarifying the charging induced nucleation in glass anode of Li-ion batteries and its enhanced performances, Nano Energy 57 (2019) 592–599

[17] Y. Hu, B. Luo, D. Ye, X. Zhu, M. Lyu, L. Wang, An Innovative Freeze-Dried Reduced Graphene Oxide Supported SnS_2 Cathode Active Material for Aluminum-Ion Batteries. Adv. Mater. 29 (48) (2017)1606132.

[18] Y. Hu, D. Ye, B. Luo, H. Hu, X. Zhu, S. Wang, L. Li, S. Peng, L. Wang, A Binder-Free and Free-Standing Cobalt Sulfide@Carbon Nanotube Cathode Material for Aluminum-Ion Batteries, Adv. Mater. 32 (2) (2018) 1703824.

[19] Y. Hu, Y. Bai, B. Luo, S. Wang, H. Hu, P. Chen, M. Lyu, J. Shapter, A. Rowan, L. Wang, Aluminum-Ion Batteries: A Portable and Efficient Solar-Rechargeable Battery with Ultrafast Photo-Charge/Discharge Rate, Adv. Energy Mater. 9 (28) (2019) 1970108.

[20] X. Xu, K. S. Hui, D. A. Dinh, K. N. Hui, H. Wang, Recent advances in nanocomposite sodium–air batteries, Materials Horizons 6 (2019) 1306–1335.

[21] Z. Genene, W. Mammo, E. Wang, M.R. Andersson, Recent Advances in n-Type Polymers for All-Polymer Solar Cells, Adv. Mater. 31 (22) (2019) 1807275.

[22] F. Liu, L. Zeng, Y. Chen, R. Zhang, R. Yang, J. Pang, L.Ding, H. Liu, W. Zhou, Ni-Co-N nanocomposite porous nanosheets on graphene paper for flexible and editable asymmetric all-solid-state supercapacitors, Nano Energy 61 (2019) 18–26.

[23] Y. Zhu, X. Ji, S. Cheng, Z.-Y. Chern, J. Jia, L. Yang, H. Luo, J. Yu, X. Peng, J. Wang, W. Zhou, M. Liu, Fast Energy Storage in Two-Dimensional MoO_2 Enabled by Uniform Oriented Tunnels, ACS Nano 13 (2019) 8, 9091–9099.

[24] F. Xiong, Q. An, L. Xia, Y. Zhao, L. Mai, H. Tao, Y. Yue, Revealing the atomistic origin of the disorder-enhanced Na-storage performance in $NaFePO_4$ battery cathode. Nano Energy 57 (2019) 608–615.

[25] X. Zhang, X. Xu, W. He, G. Yang, J. Shen, J. Liu, Q. Liu, $LiFePO_4/NaFe_3V_9O_{19}$/porous glass nanocomposite cathodes for Li^+/Na^+ mixed-ion batteries, J. Mater. Chem. A 3 (44) (2015) 22247–22257.

[26] T. M. Gür, Review of electrical energy storage technologies, materials and systems: challenges and prospects for large-scale grid storage, Energy Environ. Sci. 11 (2018) 2696–2767.

[27] J. Pan, S. Chen, D. Zhang, X. Xu, Y. Sun, F. Tian, P. Gao, J. Yang, Review of electrical energy storage technologies, materials and systems: challenges and prospects for large-scale grid storage, Adv. Funct. Mater. 28 (43) (2018)1804672.

[28] I. Bezza, V. Trouillet, A. Fiedler, M. Bruns, S. Indris, H. Ehrenberg, I. Saadoune, Understanding the lithiation/delithiation process in SnP_2O_7 anode material for lithium-ion batteries, Electrochimica Acta 252 (2017) 446–452.

[29]. J. Tian, D. Wang, Z. Shan, Improved electrochemical performances of $LiSn_2(PO_4)_3$ anode material for lithium-ion battery prepared by solid-state method, J. Power Sources 361 (2017) 96–104.

[30] W.-J. Cui, J. Yi, L. Chen, C.-X. Wang, Y.-Y Xia, Synthesis and electrochemical characteristics of NASICON-structured $LiSn_2(PO_4)_3$ anode material for lithium-ion batteries, J. Power Sources 217 (2012) 77–84.

[31] N. Bounar, A. Benabbas, P. Ropa, J.-C. Carru, Synthesis and ionic conductivity of NASICON-structured $LiTi_{2-x}Sn_x$ $(PO_4)_3$ anode material for lithium-ion batteries, Advances in Materials and Processing Technologies 3 (3) (2017) 241–249.

[32] B. Liu, Y. Xing, X. Sun, X. Liu, S.Y. Hou, Microemulsion-mediated solvothermal synthesis and characterization of $NaSn_2(PO_4)_3$ nanocubes, Mater. Lett. 63 (29) (2009) 2548–2551.

[33] P. Hu, J. Ma, T. Wang, B. Qin, C. Zhang, C. Shang, J. Zhao and G. Cui, NASICON-Structured $NaSn_2(PO_4)_3$ with Excellent High rate Properties as Anode Material for Lithium Ion Batteries, Chem. Mater. 27 (19) (2015) 6668–6674.

[34] S. Difi, A. Nassiri, I. Saadoune, M. T. Sougrati, P.-E.Lippens, Electrochemical Performance and Mechanisms of $NaSn_2(PO_4)_3$/C Composites as Anode Materials for Li-Ion Batteries. Batteries, The Journal of Physical Chemistry C 122 (21) (2018) 11194–11203.

[35] B. Zhang, T. Zeng, Y. Liu, J. Zhang, Effect of Ti-doping on the electrochemical performance of sodium vanadium (III) phosphate, RSC Adv. 8 (10) (2018) 5523–5531.

[36] X. Wang, W. Wang, B. Zhu, F. Qian, Z. Fang, Mo-doped $Na_3V_2(PO_4)_3$@C composites for high stable sodium ion battery cathode, Front. Mater. Sci. 12 (1) (2018) 53–63.

[37] M. J. Aragón, P. Lavela, G. F. Ortiz, J. L. Tirado, Benefits of Chromium Substitution in $Na_3V_2(PO_4)_3$ as a Potential Candidate for Sodium-Ion Batteries, ChemElectroChem 2 (7) (2015) 995–1002.

[38] H. Li, X. Yu, Y. Bai, F. Wu, C. Wu, L.-Y. Liu, X.-Q. Yang, Effects of Mg doping on the remarkably enhanced electrochemical performance of $Na_3V_2(PO_4)_3$ cathode materials for sodium ion batteries, J. Mater. Chem. A 3 (18) (2015) 9578–9586.

[39] M. J. Aragón, P. Lavela, G. F. Ortiz, J. L. Tirado, Effect of Iron Substitution in the Electrochemical Performance of $Na_3V_2(PO_4)_3$ as Cathode for Na-Ion Batteries, J. Electrochem. Soc. 162 (2) (2015) A3077–A3083.

[40] Z. Jiang, J. Zhu, Y. Li, Z. He, W. Meng, Y. Jiang, L. Dai, L. Wang, Effect of Sn doping on the electrochemical performance of $NaTi_2(PO_4)_3$/C composite, Ceram. Int. 44 (13) (2018) 15646–15652.

[41] M. Wang, M. Xie, Z. Zhou, Y. Huang, Z. Wang, Y. Mei, F. Wu, R. Chen, Hollow $NaTi_{1.9}Sn_{0.1}(PO_4)_3$@C nanoparticles for anodes of sodium-ion batteries with superior rate and cycling properties, Energy Technology 7 (6) (2019) 1900079.

[42] M.J. Aragón, C. Vidal-Abarca, P. Lavela, J.L. Tirado, High reversible sodium insertion into iron substituted $Na_{1+x}Ti_{2-x}Fe_x(PO_4)_3$, J. Power Sources 252 (2014)208–213.

[43] F.E. Mouahid, B.M. ettach, M. Zahir, P. Maldonado-Manso, S. Bruque, E.R. Losilla, M.A. G. Aranda, Crystal chemistry and ion conductivity of the $Na_{1+x}Ti_{2-x}Al_x(PO_4)_3$ ($0 \leq x \leq 0.9$) NASICON series, J. Mater. Chem. 10 (12) (2000) 2748–2757.

[44] P. Zhang, F. Qin, L. Zou, M. Wang, K. Zhang, Y. Lai, J. Li, Few-Layer MoS_2/C with Expanding d-Spacing as High-Performance Anode for Sodium Ion Batteries, Nanoscale 9 (33) (2017) 12189–12195.

[45] H. Liao, L. Xie, Y. Zhang, X. Qiu, S. Li, Z. Huang, H. Hou, X. Ji, Mo-doped Gray Anatase TiO_2: Lattice Expansion for Enhanced Sodium Storag, Electrochim. Acta 219 (2016) 227–234.

[46] Q. Li, Q. Wei, J. Sheng, M. Yan, L. Zhou, W. Luo, R. Sun, L. Mai, Mesoporous Li_3VO_4/C Submicron-Ellipsoids Supported on Reduced Graphene Oxide as Practical Anode for High-Power Lithium-Ion Batteries, Advanced Science 2 (12) (2015) 1500284.

[47] X. Zhang, Z. Bi, W. He, G. Yang, H. Liu, Y. Yue. Fabricating high-energy quantum dots in ultra-thin $LiFePO_4$ nanosheet using a multifunctional high-energy biomolecule–ATP, Energy Environ. Sci. 7 (2014) 2285–2294.

[48] R.C. Da Costa, A.D. Rodrigues, T.R. Cunha, J.W.M. Espinosa, P.S. Pizani, Raman scattering and phonon anharmonicity as a tool for assisting TiO_2-based ceramics synthesis, Ceram. Int. 43 (1) (2017) 116–120.

[49] X. Zhang, X. Xu, Y. Hu, G. Xu, W. He, J. Zhu, $C_{60}/Na_4FeO_3/Li_3V_2(PO_4)_3$/soft carbon qua nanocomposite superstructure for high-performance battery-supercapacitor devices, NPG Asia Mater. 12:8 (2020) (1–11).

[50] Y. Zhang, P. Zhu, L. Huang, J. Xie, S. Zhang, G. Cao, X. Zhao, Few-Layered SnS_2 on Few-Layered Reduced Graphene Oxide as Na-Ion Battery Anode with

Ultralong Cycle Life and Superior Rate Capability, Adv. Funct. Mater. 25 (3) (2014) 481–489.

[51] Y. Xu, Q. Wei, C. Xu, Q. Li, Q. An, P. Zhang, J. Sheng, L. Zhou, L. Mai, Layer-by-Layer $Na_3V_2(PO_4)_3$ Embedded in Reduced Graphene Oxide as Superior Rate and Ultralong-Life Sodium-Ion Battery Cathode, Adv. Energy Mater. 6 (14) (2016) 1600389.

[52] D. Aureau, M. Frégnaux, C. Njel, J. Vigneron, M. Bouttemy, A.-M. Gonçalves, A. Etcheberry, XPS study during a soft and progressive sputtering of a monolayer on indium phosphide by argon cluster bombardment, Surf. Interface Anal. 50 (11) (2018) 1163–1167.

[53] C. Wang, Y. Zhang, Y.Wei, L. Mei, S. Xiao, Y. Chen, XPS study of the deoxidization behavior of hydrogen in TiH_2 powders, Powder Technology 302 (2016) 423–425.

[54] Z. Wan, R. Cai, S. Jiang, Z. Shao, Nitrogen- and TiN-modified $Li_4Ti_5O_{12}$: one-step synthesis and electrochemical performance optimization, J. Mater. Chem. 22 (34) (2012) 17773–17781.

[55] W. Xia, W. Zhang. Energy Sources, Part A: Recovery, Characterization of surface properties of Inner Mongolia coal using FTIR and XPS. Energy Sources, Part A: Recovery, Utilization, and Environmental Effects 39 (11) (2017) 1190–1194.

[56] J. Li, Y. Zhang, T. Gao, J. Han, X. Wang, B. Hultman, P. Xu, Z. Zhang, G. Wu, B. Song, A confined “microreactor” synthesis strategy to three dimensional nitrogen doped graphene for high-performance sodium ion battery anodes, J. Power Sources 378 (2018)105–111.

[57] X. Ma, Y. Dai, L. Yu, B. Huang, Noble-Metal-Free Plasmonic Photocatalyst: Hydrogen Doped Semiconductors, Sci. Rep. 4 (2014) 3986 (1–7).

[58] X. Sun, Y. Guo, C. Wu, Y. Xie, The Hydric Effect in Inorganic Nanomaterials for Nanoelectronics and Energy Applications, Adv. Mater. 27 (26) (2015) 3850–3867.

[59] H. Wang, H. Wang, J. Huang, X. Zhou, Q. Wu, Z. Luo, F. Wang, Hierarchical Mesoporous/Macroporous Co-Doped NiO Nanosheet Arrays as Free-Standing anode Materials for Rechargeable Li–O_2 Batteries, ACS Appl. Mater. Interfaces 11 (47) (2019) 44556–44565.

[60] K. Zhang, X. Zhang, W. He, W. Xu, G. Xu, X. Yi, X. Yang, J. Zhu, Rational design and kinetics study of flexible sodium-ion full batteries based on binder-free composite film anodes, J. Mater. Chem. A 7 (2019) 9890–9902.

[61] X. Feng, J. He, X. Wang, G. Wang, X. Wan, H. Peng, Effect of VO_4^{3-} Substitution on the Electrochemical Properties of a $LiSn_2(PO_4)_3$ Anode Material, Chemical Research in Chinese Universities 34 (3) (2018) 444–450.

[62] A. Varzi, D. Bresser, J. von Zamory, F. Mueller, S. Passerini, $ZnFe_2O_4$-C/$LiFePO_4$-CNT: A novel high-power lithium-ion battery with excellent cycling performance, Adv. Energy Mater. 4 (10) (2014) 1400054.

[63] P. Simon, Y. Gogotsi, B. Dunn, Where Do Batteries End and Supercapacitors Begin?, Science Magazine. 343 (6176) (2014) 1210–1211.

[64] J. Liu, J. Wang, C. Xu, H. Jiang, C. Li, L. L. Zhang, J. Lin, Z. Shen, Advanced Energy Storage Devices: Basic Principles, Analytical Methods, and Rational Materials Design, Adv. Sci. 5 (1) (2018) 1700322.

[65] V. Augustyn, J. Come, M. A. Lowe, J. W. Kim, P. L. Taberna, S. H. Tolbert, H. D. Abruna, P. Simon, B. Dunn, High-rate electrochemical energy storage through Li^+ intercalation pseudocapacitance, Nat Mater. 12 (2013) 518−522.

Figure legends

Fig. 1. XRD patterns of different samples over a range of 2θ angle from (a)10 to 70° and (b) from 60 to 90°(enlarged). (c) diffraction peak contrast of (110) lattice plan. (d) Raman spectra of different samples at a range of low wavenumber from 100 to 1000 cm^{-1} and (e) Raman spectra deconvoluted by four Gaussian peaks of $T_{0.01}$-QDs/2D-NSP/H-HC sample. (f) Nitrogen adsorption-desorption isotherm and (g) BJH pore-size distribution of $T_{0.01}$-QDs/2D-NSP/H-HC sample.

Fig. 2. (a) The full XPS spectrum of $T_{0.01}$-QDs/2D-NSP/H-HC sample. High-resolution XPS spectra of Sn3d (b), Ti2p (c) and C1s (d). (e-i) The elemental mappings of $T_{0.01}$-QDs/2D-NSP/H-HC sample, tin (e), titanium (f), carbon (g),

phosphorus (h) and sodium (i).

Fig. 3. Morphology and fine texture characterizations of $T_{0.01}$-QDs/2D-NSP/H-HC sample. (a-c) SEM images. (de) TEM images. (f-i) HRTEM images. (j) TEM-EDS image. (k) The corresponding energy spectrum and elemental content. (l) The color mixing elemental mapping image: Ti (red), Na (yellow), Sn (violet), P (green) and C (blue-green).

Fig. 4. Electrochemical performance characterizations of the half cells assembled with the T_x-QDs/2D-NSP/H-HC (x=0, 0.002, 0.01, 0.02) hybrid electrodes synthesized under the different conditions and Li foil cathode. The intial charge-discharge curves at 0.1 A g^{-1} for $T_{0.01}$-QDs/2D-NSP/H-HC synthesized with (a) different heat treatment temperature for 8 h, (b) different heat treatment time at 600 °C and (c) different Ti doped content at 600 °C for 8 h. (d) Rate performance of the T_x-QDs/2D-NSP/H-HC from 0.1 A g^{-1} to 5A g^{-1}. (e) Ragone plots (energy density vs. power density) of the T_x-QDs/2D-NSP/H-HC. (f) Nyquist plots of the T_x-QDs/2D-NSP/H-HC. (g) Long cycling performance of the $T_{0.01}$-QDs/2D-NSP/H-HC at 2 A g^{-1}.

Fig. 5. Electrochemical performance comparison of $T_{0.01}$-QDs/2D-NSP/H-HC//PNVP full batteries before and after prelithiation. (ac) Photos of brightness contrast of the lit LED bulb driven by the full batteries. (bd) Charge and discharge curve contrast. (e) Rate performance of the full battery after prelithiation. (f) Ragone plot comparison of

energy and power density. (g) Long cycling performance of the full battery after prelithiation at 2 C.

Fig. 6. The energy storage mechanism of different batteries. (a) The CV curves, (b) plots of log (sweep rate) versus log (peak current) and (c) capacitive contribution of the half cell assembled with the $T_{0.01}$-QDs/2D-NSP/H-HC anode and Li foil cathode at various sweep rates. (d) The CV curves, (e) plots of log (sweep rate) versus log (peak current) and (f) capacitive contribution of the $T_{0.01}$-QDs/2D-NSP/H-HC//PNVP full battery before prelithiation at various sweep rates. (g) The CV curves, (h) plots of log (sweep rate) versus log (peak current) and (i) capacitive contribution of the $T_{0.01}$-QDs/2D-NSP/H-HC//PNVP full battery after prelithiation at various sweep rates.

Highlights

► Metal Ti quantum chain-inlaid 2D $NaSn_2(PO_4)_3$/H-doped hard carbon hybrid electrode

► This electrode possesses unique sandwich and hierarchically meso-macroporous structures.

► The mixed-ion full battery exhibits ultrahigh energy and power densities (555 Wh

Kg^{-1}/804 W Kg^{-1}).

► The mixed-ion storage mechanism of this hybrid electrode is evaluated.